Overview of Physics Results from the National Spherical Torus Experiment

S.A. Sabbagh[1], J-W. Ahn[2], J. Allain[3], R. Andre[4], A. Balbaky[1], R. Bastasz[5], D. Battaglia[4], M. Bell[4], R. Bell[4], E. Belova[4], J. Berkery[1], R. Betti[6], J. Bialek[1], T. Bigelow[2], M. Bitter[4], J. Boedo[7], P. Bonoli[8], A. Boozer[1], A. Bortolon[9], D. Brennan[10], J. Breslau[4], R. Buttery[11], J. Canik[2], G. Caravelli[12], C. Chang[4], N. Crocker[13], D. Darrow[4], B. Davis[4], L. Delgado-Aparicio[4], A. Diallo[4], S. Ding[14], D. D'Ippolito[15], C. Domier[16], W. Dorland[17], S. Ethier[4], T. Evans[11], J. Ferron[11], M. Finkenthal[12], J. Foley[18], R. Fonck[19], R. Frazin[20], E. Fredrickson[4], G. Fu[4], D. Gates[4], S. Gerhardt[4], A. Glasser[21], N. Gorelenkov[4], T. Gray[2], Y. Guo[14], W. Guttenfelder[4], T. Hahm[4], R. Harvey[22], A. Hassanein[3], W. Heidbrink[9], K. Hill[4], Y. Hirooka[23], E.B. Hooper[24], J. Hosea[4], D. Humphreys[11], K. Indireshkumar[4], F. Jaeger[2], T. Jarboe[21], S. Jardin[4], M. Jaworski[4], R. Kaita[4], J. Kallman[4], O. Katsuro-Hopkins[1], S. Kaye[4], C. Kessel[4], J. Kim[25], E. Kolemen[4], G. Kramer[4], S. Krasheninnikov[7], S. Kubota[13], H. Kugel[4], R.J. La Haye[11], L. Lao[11], B. LeBlanc[4], W. Lee[26], K. Lee[16], J. Leuer[11], F. Levinton[18], Y. Liang[16], D. Liu[9], N. Luhmann Jr. [16], R. Maingi[2], R. Majeski[4], J. Manickam[4], D. Mansfield[4], R. Maqueda[18], E. Mazzucato[4], A. McLean[2], D. McCune[4], B. McGeehan[26], G. McKee[19], S. Medley[4], E. Meier[24], J. Menard[4], M. Menon[27], H. Meyer[28], D. Mikkelsen[4], G. Miloshevsky[3], D. Mueller[4], T. Munsat[29], J. Myra[15], B. Nelson[21], N. Nishino[30], R. Nygren[5], M. Ono[4], T. Osborne[11], H. Park[25], J. Park[4], Y. Park[1], S. Paul[4], W. Peebles[13], B. Penaflor[11], C. Phillips[4], A. Pigarov[7], M. Podesta[4], J. Preinhaelter[31], R. Raman[21], Y. Ren[4], G. Rewoldt[4], T. Rognlien[24], P. Ross[4], C. Rowley[4], E. Ruskov[9], D. Russell[15], D. Ruzic[20], P. Ryan[2], M. Schaffer[11], E. Schuster[32], F. Scotti[4], K. Shaing[19], V. Shevchenko[28], K. Shinohara[33], V. Sizyuk[3], C. Skinner[4], A. Smirnov[22], D. Smith[19], P. Snyder[11], W. Solomon[4], A. Sontag[2], V. Soukhanovskii[24], T. Stoltzfus-Dueck[4], D. Stotler[4], B. Stratton[4], D. Stutman[12], H. Takahashi[4], Y. Takase[34], N. Tamura[23], X. Tang[35], G. Taylor[4], C. Taylor[3], K. Tritz[12], D. Tsarouhas[3], M. Umansky[24], J. Urban[31], E. Untergberg[11], M. Walker[11], W. Wampler[5], W. Wang[4], J. Whaley[5], R. White[4], J. Wilgen[2], R. Wilson[4], K.L. Wong[4], J. Wright[8], Z. Xia[16], D. Youchison[5], G. Yu[7], H. Yuh[18], L. Zakharov[4], D. Zemlyanov[3], G. Zimmer[4], S.J. Zweben[4]

[1]Columbia University, New York, NY, USA
[2]Oak Ridge National Laboratory, Oak Ridge, TN, USA
[3]Purdue University, Purdue, IA, USA
[4]Princeton Plasma Physics Laboratory, Princeton, NJ, USA
[5]Sandia National Laboratory, Albuquerque, NM, USA
[6]University of Rochester, Rochester, NY, USA
[7]University of California at San Diego, San Diego, CA, USA
[8]Massachusetts Institute of Technology, Cambridge, MA, USA
[9]University of California at Irvine, Irvine, CA, USA
[10]University of Tulsa, Tulsa, OK, USA
[11]General Atomics, San Diego, CA, USA
[12]Johns Hopkins University, Baltimore, MD, USA
[13]University of California at Los Angeles, Los Angeles, CA, USA
[14]Institute of Plasma Physics Chinese Academy of Sciences, Hefei, P.R. China
[15]Lodestar Research Corporation, Boulder, CO, USA
[16]University of California at Davis, Davis, CA, USA
[17]University of Maryland, College Park, MD, USA
[18]Nova Photonics, Inc., Princeton, NJ, USA
[19]University of Wisconsin,Madison,WI, USA
[20]University of Illinois at Urbana-Champaign, Urbana, IL, USA
[21]University of Washington, Seattle, WA, USA
[22]CompX, Del Mar, CA, USA
[23]National Institute for Fusion Science, Oroshi, Toki, Gifu, Japan
[24]Lawrence Livermore National Laboratory, Livermore, CA, USA
[25]POSTECH, Pohang, Korea
[26]Dickinson College, Carlisle, PA, USA
[27]Think Tank Inc., Silver Springs, MD, USA
[28]Culham Center for Fusion Energy, Abingdon, Oxfordshire, UK

[29]University of Colorado at Boulder, Boulder, CO, USA
[30]Hiroshima University, Hiroshima, Japan
[31]Institute of Plasma Physics, AS CR, Prague, Czech Republic
[32]Lehigh University, Bethlehem, PA, USA
[33]Japan Atomic Energy Agency, Naka, Ibaraki, Japan
[34]University of Tokyo, Tokyo, Japan
[35]Los Alamos National Laboratory, Los Alamos, NM, USA

E-mail contact of main author: sabbagh@pppl.gov

Abstract. Research on the National Spherical Torus Experiment, NSTX, targets physics understanding needed for extrapolation to a steady-state ST Fusion Nuclear Science Facility, pilot plant, or DEMO. The unique ST operational space is leveraged to test physics theories for next-step tokamak operation, including ITER. Present research also examines implications for the coming device upgrade, NSTX-U. A τ_E scaling appropriate for varied wall conditions exhibits a strong improvement of $B_T\tau_E$ with decreased electron collisionality produced by lithium (Li) wall conditioning. Nonlinear microtearing simulations match experimental electron diffusivity quantitatively and predict reduced electron heat transport at lower collisionality. Beam-emission spectroscopy measurements indicate the poloidal correlation length of pedestal turbulence ~ 10 ρ_i increases at higher electron density gradient and lower T_i gradient. Plasma characteristics change nearly continuously with increasing Li evaporation and ELMs stabilize due to edge density gradient alteration. Global mode stability studies show stabilizing resonant kinetic effects are enhanced at lower collisionality. Combined radial and poloidal field sensor feedback controlled n = 1 perturbations and improved stability. The disruption probability due to unstable RWMs is reduced at high $\beta_N/l_i > 11$ consistent with low frequency MHD spectroscopy measurements of mode stability. Greater instability seen at intermediate β_N is consistent with decreased kinetic RWM stabilization. A model-based RWM state-space controller produced long-pulse discharges exceeding β_N = 6.4 and β_N/l_i = 13. Precursor analysis shows 98% of disruptions can be predicted with 10ms warning and a false positive rate of only 6%. Disruption halo currents rotate toroidally and can have significant toroidal asymmetry. Global kinks cause measured fast ion redistribution. Full-orbit calculations show redistribution from the core outward and toward $V_{||}/V = 1$ where destabilizing CAE resonances are expected. Applied 3D fields alter GAE characteristics. The snowflake divertor configuration enhanced by radiative detachment shows large reductions in both steady-state and ELM heat fluxes (steady-state peak values down from 7 MW/m^2 to less than 1 MW/m^2). Toroidal asymmetry of heat deposition is observed during ELMs or by 3D fields. Coaxial helicity injection has reduced the inductive startup flux, with plasmas ramped to 1MA requiring 35% less inductive flux. Non-inductive current fraction (NICF) up to 65% is reached experimentally with NBI at I_p = 0.7 MA and between 70 – 100% with high harmonic fast wave application at I_p = 0.3 MA. NSTX-U scenario development calculations project 100% NICF for a large range of $0.6 < I_p$ (MA) < 1.35.

1. Introduction

Research on the National Spherical Torus Experiment, NSTX, targets the development of predictive physics understanding needed to extrapolate plasma transport, stability, power handling, non-inductive sustainment, and advanced control techniques confidently toward a steady-state Fusion Nuclear Science Facility (ST-FNSF) / Component Test Facility (ST-CTF) [1-2], a pilot plant [3], or DEMO based on the ST [4]. The unique ST operational space and device geometry are leveraged to extend and test physics theories and technological solutions for next-step ST and tokamak operation, including ITER. Recent research also examines implications for the coming device upgrade, NSTX-U [5] that will double the toroidal field, B_t, plasma current, I_p, and NBI heating power to produce yet unexplored, hotter, high β ST plasmas at reduced collisionality, ν, for several current diffusion times (5s pulses). Understanding the dependence of high β plasma transport and stability at reduced ν is critical to determine the size and control capabilities needed for an ST-FNSF/CTF. Edge recycling can significantly affect energy confinement and stability, and lithium (Li) wall conditioning is investigated in these roles. Advanced instability control and disruption warning techniques are required for disruption avoidance. Innovative divertor configurations are needed to handle the high heat and particle fluxes. High non-inductive fraction operation is required to reach a key milestone of demonstrating routine fully non-inductive operation. Understanding the impact of non-axisymmetric effects (e.g. applied 3-D fields) on stability and first wall heat fluxes is needed. Filling the knowledge gaps for these critical areas comprises present NSTX research, and these topics are addressed in the present paper.

2. Transport and Stability Physics at Reduced Collisionality

2.1. Energy Confinement Dependence on Collisionality

Lower collisionality has been obtained in H-mode plasmas via lithium (Li) conditioning of first wall components. An increase in energy confinement time, τ_E, has also been reported, most notably in the electron channel [6]. A unified scaling of τ_E using engineering parameters in discharges with/without lithium wall conditioning (lithiated/unlithiated) has not been found. However, such a scaling has been produced by considering a more profound underlying collisionality variation that unifies results for differing wall conditions and that exhibits a strong improvement of B_T-normalized energy confinement with decreasing ν^* [7]. Variations including gyrofrequency are accounted by normalizing τ_E as $B_T\tau_E$ while minimizing q and $<\beta_t>$ variations (data constrained to $2 < q(r/a=0.5) < 2.5$, and $8.5 < <\beta_t> < 12.5\%$). The data set spans a factor of four variation in normalized electron collisionality, ν^*_e (at r/a=0.5). The scaling $B_T\tau_E \propto \nu^{*\,-0.79}_e$ is found for all discharges (FIG. 1), and a similar strong inverse scaling $\propto \nu^{*\,-0.67}_e$ is found for lithiated discharges alone. Local T_e variation due to profile broadening is the most influential factor in varying ν^*_e. Including a variation of the normalized gyroradius ρ^* yields a considerably stronger favorable increase of $B_T\tau_E$ with decreased ν^*_e, assuming either a Bohm, or gyroBohm dependence [7]. Ion transport, near neoclassical at higher collisionality, is more anomalous at lower collisionality due to growth of hybrid TEM/KBM modes in the plasma outer region [8].

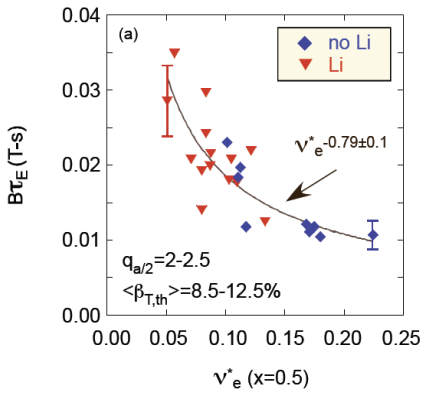

FIG. 1. Normalized τ_E vs. ν^*_e for lithiated/unlithiated plasmas.

2.2. Gyrokinetic Simulations of Electron Thermal Transport

The broad ST parameter space yields a wide-range of possible microinstabilities, providing a unique laboratory for developing an integrated understanding of transport. The dependence of electron thermal transport on electron collisionality, ν_{ei}, is examined for plasmas with different underlying microinstabilites. Plasmas with sufficiently high electron beta, $\beta_e \sim 3\%$ are computed (linear calculations) to be unstable to microtearing modes. Low β_e plasmas are below the microtearing threshold and are instead predicted to be unstable to ETG modes. Nonlinear gyrokinetic simulations give the magnitude and scaling of both microtearing and ETG transport. These have shown success in quantitatively reproducing electron thermal transport and understanding its dependence on collisionality [9]. Nonlinear microtearing simulations predict reduced electron heat transport at lower ν and match the experimental electron diffusivity, χ_e, quantitatively (FIG. 2a). The computed scaling $\chi_e \sim \nu_e^{1.1}$ is consistent with the experimentally derived $B_t\tau_E \sim \nu^{*\,-0.79}_e$ (section 2.1). The magnetic turbulence leads to stochastic field lines and computed transport is dominated by magnetic flutter with high $\delta B_r/B \sim 0.1\%$ (FIG. 2b). At low β_e, nonlinear simulations predict in some cases that ETG instabilities are responsible for significant electron transport. However, a negligible dependence of electron transport with collisionality is found, which is inconsistent with the strong dependence of χ_e on ν_e found experimentally. Accumulation of small differences in other parameters may lead to the overall change in confinement. For

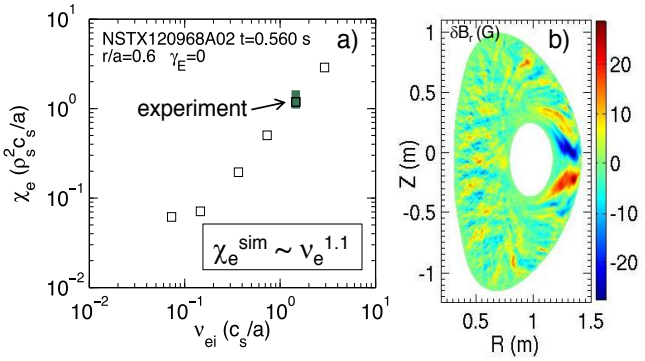

FIG. 2. a) Computed electron diffusivity vs. electron collisionality; b) poloidal cross section plot of computed radial B field fluctuation.

example, simulations at slightly different radii illustrate the predicted ETG transport is sensitive to local variations in density gradient [10].

In L-mode, a computed reduction of χ_i and χ_e is consistent with *ExB* shear stabilization of low-*k* turbulence, which in turn reduces the high-*k* fluctuations nonlinearly, consistent with high-*k* measurements [11]. RF-heated L-mode plasmas have also been used to investigate ETG turbulence physics. Electron internal transport barriers (e-ITBs) have been found to occur with strong negative magnetic shear ($s < -0.5$). Both the large local electron temperature gradients (much larger than the linear ETG threshold) and the small turbulence intensity found from high-k scattering measurements are strongly correlated with the largest negative magnetic shear [12]. Non-local GYRO simulations verify that ETG turbulence and transport are suppressed with strong negative magnetic shear in the region of the e-ITB [13].

2.3. Resistive Wall Mode Stability Dependence on Collisionality

Past NSTX research established a new understanding of resistive wall mode (RWM) stability by making quantitative correlation between experiments reaching RWM marginal stability and kinetic RWM stabilization theory [14,15]. This physics model has important implications for next-step devices operating at reduced collisionality, ν. Stabilizing effects of collisional dissipation are reduced at lower ν, but stabilizing resonant kinetic effects can be enhanced. Stronger RWM stabilization occurs near broad dissipative kinetic resonances (which depend on the plasma rotation profile) and increases with decreasing ν, but in stark contrast has almost no dependence on ν when the plasma is off-resonance (FIG 3). In this figure, ν_{exp} and ω_ϕ^{exp} represent experimental values in high beta plasmas and extrapolated kinetic RWM stability calculations are made using the MISK code [16]. Experiments utilizing $n = 1$ active MHD spectroscopy [17] diagnosis, which uses $n = 1$ resonant field amplification (RFA) to measure RWM stability [18], show the theoretically expected gradient in kinetic RWM stability at high $5.5 < \beta_N/l_i < 13.5$ (most above the $n = 1$ ideal no-wall stability limit) (FIG. 4).

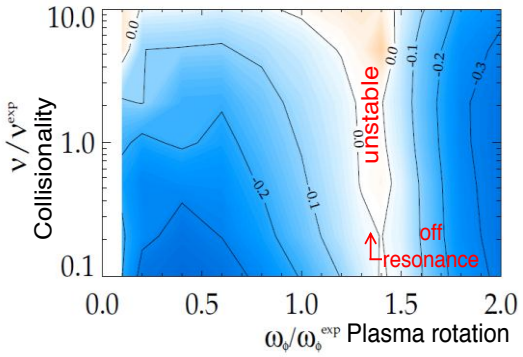

FIG 3. MISK computed kinetic RWM n = 1 stability vs. collisionality and plasma rotation.

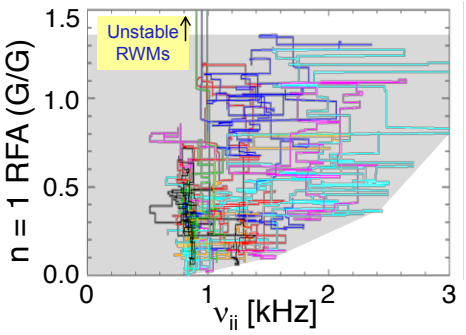

FIG. 4. n = 1 RFA amplitude vs. ν_{ii}, showing a relatively large change at low RFA ("on resonance") vs. almost no change at high RFA.

RFA amplitude trajectories are shown for 20 discharges for which ion collisionality, ν_{ii}, is varied by a factor of 3.75. At high $n = 1$ RFA amplitude (upper boundary) the plasma is off-resonance and there is almost no change in RWM stability (indicated by the $n = 1$ RFA amplitude) vs. ν_{ii}. At low $n = 1$ RFA amplitude (lower boundary) the plasma has greater stabilization by kinetic resonances shown by a clear increase in RWM stability (decrease in $n = 1$ RFA amplitude) as ν_{ii} is decreased. Here, ν_{ii} is averaged over $0.55 < \psi/\psi_n < 0.75$.

3. Transport and Stability of the H-mode Pedestal

3.1. Effects of Lithium Wall Conditioning and ELM Stabilization

Plasma characteristics change nearly continuously with increasing Li evaporation [19] with no Li accumulation in the core [20]: global energy confinement parameters improve and edge transport declines [21], ELM frequency is reduced, or the mode stabilizes completely [22]. The ELM avoidance mechanism is clarified by profile and stability analysis. The Li coating reduces density and its gradient near the separatrix. The density profile is continuously

manipulated via the amount of Li evaporation and resulting recycling control. The bootstrap current and ∇p near the separatrix are reduced solely by the density change; ∇T is unaffected. This leads to computed stabilization of kink/peeling modes thought to be responsible for ELMs. This allows the H-mode edge transport barrier to expand further such that peeling stability improves as a result of the inward shift of the bootstrap current. A beneficial facet is the continued growth of the edge transport barrier width, leading to 100% higher pressure near the top of the n_e profile barrier with high pre-discharge Li evaporation [23].

Data from liquid lithium divertor (LLD) discharges was analysed to consider whether there is a net effect on discharges over the range of total deposited Li. Examination of τ_E versus ITER H-97L scaling indicates that performance was constant throughout the run, consistent with the hypothesis that the quality of the Li surface layers impact performance. Surface analysis experiments show oxide coverage of plasma facing components (PFCs) is expected in 20-200 s from residual H_2O and other vacuum gases at typical between-discharge pressures ~1e-7 Torr. These short observed reaction times motivate flowing Li PFCs [24]. In laboratory experiments, the role of oxygen is found to be key to understanding deuterium retention of Li-coated graphite as expected from quantum-classical simulations [25].

3.2. Pedestal Width Scaling and ELM Stability Calculations

Edge pedestal profiles and associated ELM stability are important for achieving high core fusion gain in next-step devices. Peeling-ballooning modes are hypothesized to set an upper limit on the pedestal pressure. The stability of equilibria similar to those described in section 3.1 is computed using the ELITE stability code for $n = 3, 6, 9, 12, 15$ during the last part of the ELM cycle (FIG. 5). Experimental current density and pressure gradient points are shown using the Sauter and XGC0 [26] current models. Results indicate that the pedestal pressure is limited by the proximity to the kink/peeling instability limit. The XGC0 calculation of the bootstrap current is 20 - 30% larger than that of the Sauter model and puts the experimental point closer to the kink/peeling instability limit. PEST calculations of $n = 2 - 4$ modes indicate a maximum growth rate for the $n = 3$ mode. The pedestal width is thought to be set by kinetic ballooning modes [27]. This scales with $(\beta_p^{ped})^{0.5}$), where is β_p^{ped} the local poloidal beta measured at the pedestal. This scaling has been reported in several tokamaks, but present NSTX data indicates a significantly stronger scaling, closer to linear in β_p^{ped} (FIG. 6) [28].

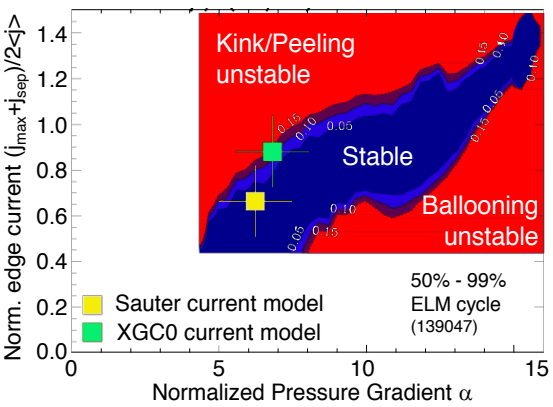

FIG. 5. Contours of peeling-ballooning mode growth rate normalized to 1/2 of the ion diamagnetic frequency, $\omega_i^*/2$, vs. normalized pressure gradient and normalized current density.

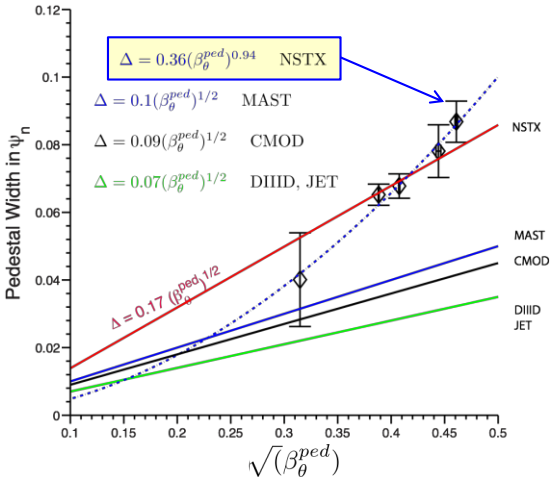

FIG. 6. Pedestal width vs. $(\beta_p^{ped})^{0.5}$), showing a near linear dependence on β_p^{ped} in NSTX.

3.3. Turbulence Measurements and Characterization in the Pedestal Region

Beam-emission spectroscopy (BES) [29] measurements have been used to measure spatial and temporal properties of ion-scale turbulence in ELM-free H-mode discharges. In the steep gradient region (the lower portion) of the pedestal, measured poloidal correlation lengths of the turbulence, $L_p \sim 10\,\rho_i$, wavenumbers $k_\theta \rho_i \sim 0.2$, and normalized decorrelation time

$\tau_d/(a/c_s) \sim 5$, where c_s is the sound speed. The L_p increases and k_θ decreases at higher ∇n_e and lower ∇T_i. The observed dependencies are most consistent with turbulence caused by trapped electron instabilities, partially consistent with KBM and microtearing modes, and least consistent with ITG turbulence [30].

Investigations were also conducted in ELMing plasmas examining the region at the top of the pedestal. Characterization of radial edge density fluctuations during the time period between ELMs (inter-ELM phases) is made possible by an array of fixed-frequency quadrature reflectometers in the pedestal region [31]. The poloidal spatial structure of these fluctuations is measured by BES. The radial correlation length increases at the top of the pedestal by a factor of 2 during the last 50% of the ELM cycle reaching $7\rho_i$, implying increased radial transport. In contrast, the correlation length remains unchanged through the ELM cycle in the steep gradient region. BES measurements also show a large, and relatively constant poloidal correlation length over the ELM cycle [28].

The edge density fluctuations in the pedestal region during the ELM cycle clearly show anisotropic fluctuations and spatial scales $2/\lambda_\perp \rho_i^{ped}$ ranging from 0.2 to 0.7 and propagate in the ion diamagnetic drift direction at the pedestal top, indicative of ion-scale microturbulence compatible with ITG (including hybrid TEM) and/or KBM instabilities. Group velocities determined from the time lags between BES channels are measureably smaller than the $E_r \times B_{||}$ velocities (inferred from CHERS carbon ion distribution force balance) at the pedestal top, and are in the electron diamagnetic direction. This is contrary to observations on DIII-D where both velocities have the same direction [28]. The measured density fluctuation correlation lengths (radial: 2 – 4 cm; poloidal: 10 – 14 cm) were compared to nonlinear gyrokinetic simulations (XGC1 code) [32] (FIG. 7). In these simulations, which consider ion dynamics and do not consider collisions and flows, electrostatic potential fluctuations form with correlation lengths matching the experimentally measured values.

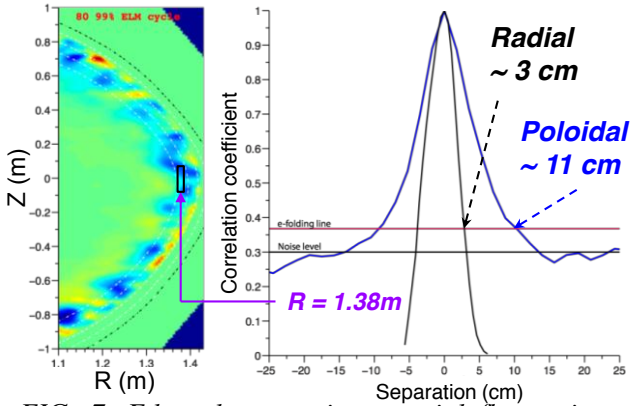

FIG. 7. Edge electrostatic potential fluctuations computed from XGC1 yield radial and poloidal correlation lengths in the range of measured values from reflectometry and BES diagnostics.

4. Macroscopic stability and control at high β, disruption prediction and characteristics

4.1. High Beta Operation and Reduced Disruptivity

Next-step STs and steady-state advanced tokamaks both aim to operate continuously at high normalized beta, $\beta_N \equiv 10^8 \langle \beta_t \rangle aB_0/I_p$, ($\beta_t \equiv 2\mu_0 \langle p \rangle / B_0^2$) and high non-inductive current fraction. High bootstrap current fraction produces a broad current profile yielding low plasma internal inductance, l_i. This is favourable for efficient non-inductive operation, but is generally unfavourable for global MHD stability, reducing the ideal $n = 1$ no-wall beta limit, $\beta_N^{no\text{-}wall}$. Past high β_N operation with l_i typically in the range $0.6 < l_i < 0.8$ has an $n = 1$ $\beta_N^{no\text{-}wall}$ computed by the DCON code to be 4.2 – 4.4 [33]. Operation at $\beta_N/l_i > 13.5$ ($\beta_N > 6.5$) has now been demonstrated transiently, with pulse-averaged β_N (averaged over constant plasma current), $\langle \beta_N \rangle_{pulse} > 5.5$ in low l_i plasmas in the range $0.4 < l_i < 0.6$ with active $n = 1$ mode control (FIG. 8). Pulse-averaged values of (l_i, β_N) now intercept the higher l_i portion of the planned operational ranges for ST-CTF and ST Pilot plants. The $\beta_N^{no\text{-}wall}$ at low l_i is significantly reduced and β_N now exceeds the DCON computed value by up to a factor of two. The disruption probability due to unstable RWMs was reduced from 48% in initial low l_i experiments to 14% with this control, and remarkably, reduced disruption probability was observed in plasmas at high $\beta_N/l_i > 11$. Disruptions occurred more frequently at intermediate

values of β_N/l_i. This agrees with active MHD spectroscopy diagnosis, used to determine the proximity to marginal stability [18] (FIG. 9). The RFA of an applied rotating n =1 seed field reaches a broad peak near β_N/l_i = 10 and decreases at higher values of β_N/l_i, indicating increased mode stability. This positive result is presently thought to be related to proximity to broad resonances in plasma rotation providing kinetic stabilization of the RWM [14,15].

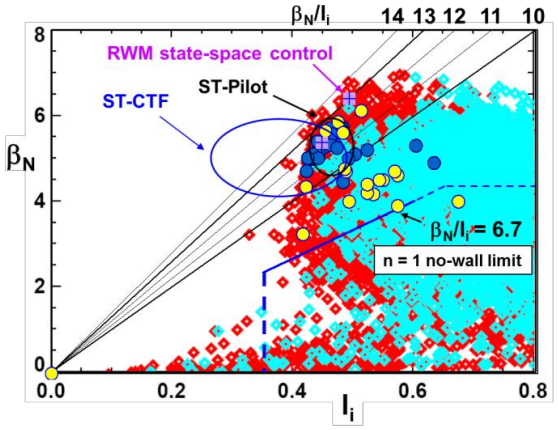

FIG. 8. High β_N, low l_i operational space. Red/cyan points indicate plasmas with/without n=1 active RWM control. Blue circles indicate stable long pulse plasmas with active RWM control; yellow circles indicate disruptions.

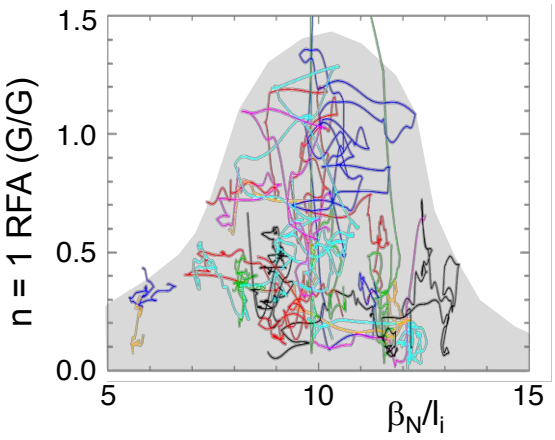

FIG. 9. n = 1 resonant field amplification during high β discharges using active MHD spectroscopy, indicating improved stability at high β_N/l_i.

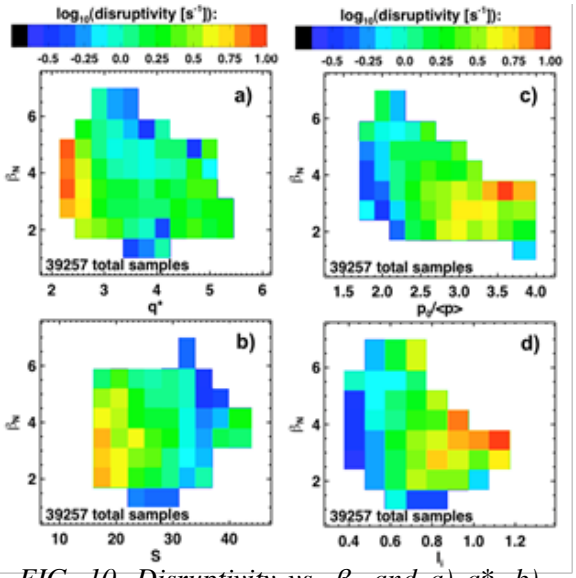

FIG. 10. Disruptivity vs. β_N and a) q, b) shape factor, c) pressure peaking, and d) l_i.*

In addition to dedicated experiments, a large database of disruption rate and disruptivity statistics, spanning 2006 - 2010 operation, has been analyzed more generally [34]. FIG. 10 shows disruptivity as a function of β_N and $q^* \equiv \varepsilon\pi a B_T(1+\kappa^2)/\mu_0 I_p$, pressure peaking factor, $F_p \equiv p(0)/\langle p\rangle$, plasma shaping factor, $S \equiv q_{95} I_p/aB_T$, and l_i. No clear increase is found in disruptivity at increased β_N and $l_i < 0.8$. Significant increases in disruptivity are found for $q^* < 2.4$, at low plasma shaping, and at high values of F_p, and l_i, each of which are generally expected. Increased S, and decreased F_p typically beneficial for stability, are also shown to yield reduced disruptivity.

NTM marginal island width results show the relative importance of the enhanced stabilizing curvature effect at low aspect ratio yielding less susceptibility to NTM onset even near marginal classical tearing stability index. Low aspect ratio advantages are confirmed by both a larger characteristic small island size for stabilization and the presence of a significant stabilizing curvature effect, making NTMs harder to excite [35]. Coherent edge harmonic oscillations at 2-8 kHz with n = 4-6 have been observed in ELM-free plasmas. These oscillations have little effect on particle or impurity transport in contrast to EHOs in DIII-D. The possibility of actively driving the EHOs using HHFW has been investigated using IPEC, which indicates that EHOs can be amplified by optimizing the HHFW for n = 4 – 6 [36].

4.2. Dual-field Component Active RWM Control and Model-based RWM Controllers

Two approaches for improved RWM control have been used and studied. First, combined use of 24 radial and 23 poloidal field RWM sensors with proportional gain feedback provided

control of n = 1 modes [18]. Modelled feedback evolution agrees with experiment for radial sensor variations examined (FIG. 11), and shows the optimal gain is 2.5 times greater than the value used in experiments. The second approach is a model-based state space controller [37] using a state derivative feedback algorithm [38] and incorporating unstable RWM currents

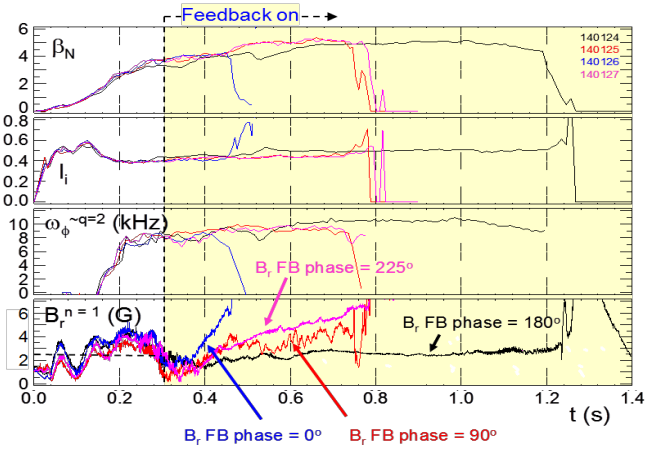

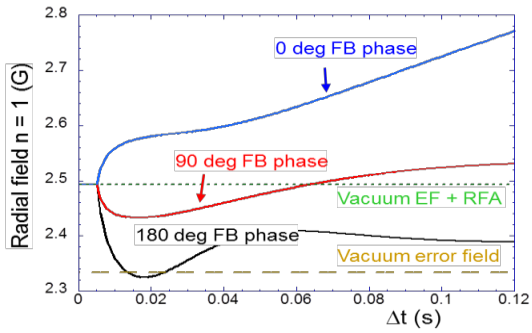

FIG. 11. RWM B_R sensor feeback phase variation with combined radial/poloidal field sensor feedback (a) experiment, (b) theory.

and those induced in nearby 3D conducting structure. Testing this physics is especially important for ITER [39] and high neutron output devices where greater control coil shielding will be needed. Using a number of states equal or greater than required by Hankel singular value analysis (7 here) provides sufficient 3D conducting structure current detail to match experimental sensors. Open-loop comparisons between sensor measurements and the RWM state space control (RWMSC) model show agreement with a sufficient number of states and improved agreement when 3D wall model details (e.g. NBI ports) were added (FIG. 12). Control was demonstrated to sustain long pulse, high β_N discharges with $n = 1$ fields applied that normally disrupt the plasma [18]. This controller was used for RWM stabilization in long-pulse plasmas (limited by coil heating constraints) reaching near maximum β_N/l_i = 13.4 (shown in FIG. 8).

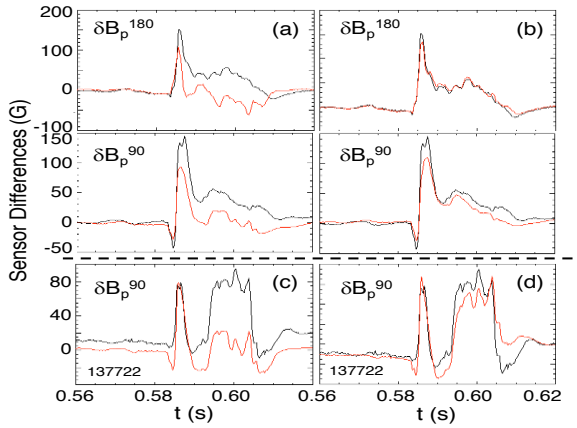

FIG. 12. Open-loop comparison of RWM sensor subset with RWMSC observer: a) 2 states, b) 7 states, c) without, and d) with the inclusion of the NBI port (7 states).

4.3. Disruption Detectability, Halo Current Characteristics and Dynamics

An extensive database study has been conducted to determine the detectability of disruptions based on multiple-input criteria [34]. Quantitative evaluation of the levels of measured input, including low frequency n = 1 MHD amplitude and neutron emission are compared to a rapidly-evaluated slowing-down model, ohmic current drive power, and plasma vertical motion (all able to be evaluated in real-time). These are determined to maximize disruption detectability, while minimizing false positives. Results illustrate that no single diagnostic dominates the detection algorithm; a combination of signals is required. In total, 17 threshold tests are computed and a weighted sum is evaluated every 2 ms for ~1700 disruptive discharges tested. A flag noting that a

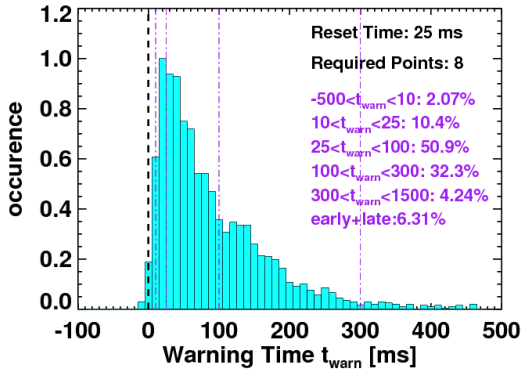

FIG. 13. Histogram of warning times computed for 1700 disruptive plasmas.

disruption is imminent is set when the single weighted sum is sufficiently large. This approach has shown high success. FIG. 13 illustrates a histogram of the warning times that this approach finds (reset time of 25 ms, eight points required for a positive flag). A total of 98% of the disruptions are flagged with at least 10 ms warning, with ~6% false positives. The number of missed warnings found are largely due to locked modes and RWMs.

Disruption-induced halo currents are observed with halo current fractions up to 25% and significant toroidal asymmetry (peaking factor up to 6) [40]. The currents are measured using an array of six shunt tiles mounted on the divertor floor. An n = 1 current asymmetry is common and can rotate toroidally (up to 7 transits; 2-3 more common) at 0.5-2 kHz. The number of toroidal transits decreases with increasing halo current magnitude. The dominant structure of the halo current is a single, toroidally localized lobe. Typical full width at half maxima for these lobes is 2-4 radians, and the rotation frequency and spatial width can vary rapidly during the disruption. The toroidal rotation of the halo currents can also be non-monotonic, with reversals in the change of the toroidal phase [34].

5. Energetic Particle Population, Modes, and 3D Field Effects

5.1. Fast ion phase space redistribution and effects on low and high frequency MHD

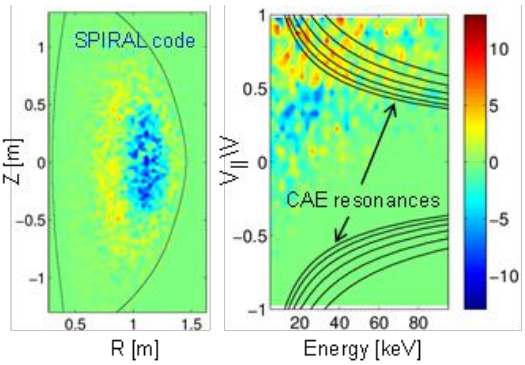

FIG. 15. Fast ion redistribution by saturated kink mode activity.

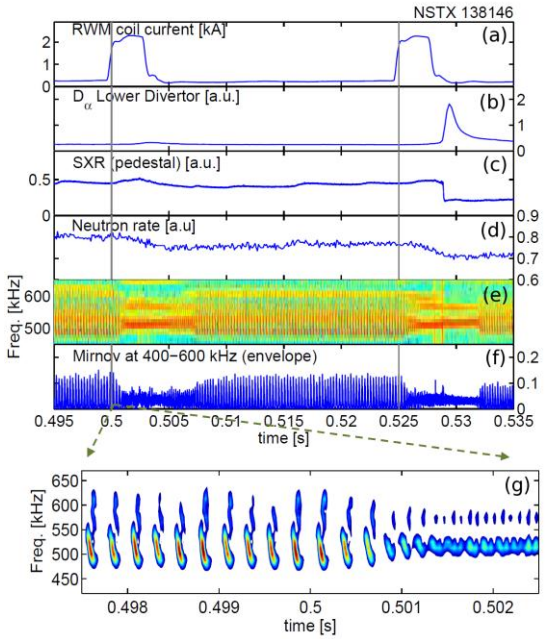

FIG. 14. GAE activity modification during applied n=3 fields: (e-f) magnetic fluctuation spectrum and rms signal amplitude from pickup coils. (g) frequency evolution at t ~ 0.5 s

TAE avalanches and associated neutron rate reduction studies, previously restricted to L-mode plasmas, are now expanded to H-mode plasmas with density profiles allowing reflectometer measurements. Prompt fast ion losses computed from ORBIT code calculations are negligible and cannot explain the observed neutron rate reduction. Instead, the simulations predict the TAE activity to cause fast ion energy scattering, causing a small (3-5%) net decrease in fast ion β. This, and the redistribution of fast ions to regions of lower density, can account for most of the measured decrease in neutron rate. The fast ion energy loss is comparable to the estimated energy lost by Alfvén wave damping during the burst [41].

Low frequency n = 1 global kinks cause fast ion redistribution as measured by a fast ion D_α diagnostic . This new observation in turn leads to Alfvénic mode destabilization. Full-orbit code (SPIRAL) calculations have been performed with an ideal kink radial mode structure validated by soft X-ray data. The simulation indicates that fast ion redistribution occurs from the core outward, and toward $V_{||}/V$ = 1 where CAE resonances are expected, leading to observed CAE destabilization (FIG. 15).

Applying n = 3 field pulses alters the stability and behavior of high frequency instabilities (FIG. 14). Beam ions drive persistent bursting/chirping modes between 400-700 kHz. The modes are apparently Global Alfven eigenmodes (GAE) with n = 7-9. When the n = 3 pulse is applied, the GAE burst frequency triples, the mode amplitude halves, and the frequency sweep extent decreases from 100 kHz to 40 kHz. SPIRAL code analysis

indicates a depletion of the portion of fast ion distribution phase space that drives the GAE instabilities. This result may lead to a control approach for fast-particle driven instabilities.

Stabilizing effects of energetic particles have been computed using MISK to play a significant role in the RWM stability of NSTX plasmas [42]. Extrapolation to ITER Advanced Scenario plasmas shows that the stabilizing effect of alpha particles will be required at expected ITER plasma rotation levels, but ITBs may alleviate the needed α stabilization by strengthening the stabilizing ion precession drift resonance [18].

5.2. Measurement and Structure of Internal CAE and GAE Modes

Identification of observed Alfvénic mode activity such as GAE, CAE is essential to understanding how the modes will affect the plasma, as they will have different effects on resonant particle orbits. Detailed measurements of high frequency AE amplitude and mode structure were made for the first time in the core of NBI-heated H-mode plasmas [43]. Modes are identified by comparing frequency and n numbers with local Alfvén dispersion relations. Observed CAE modes have higher frequencies ($f > \sim 600$ kHz) and smaller toroidal mode numbers ($|n| \leq 5$) than GAEs ($f < \sim 600$ kHz, $n = -6 - -8$) and are strongly core localized. GAE modes peak toward the plasma core but have much broader radial extent.

6. Heat Flux Mitigation by the Snowflake Divertor and 3D Effects

6.1. Radiative Snowflake Divertor

The standard radiative divertor solution is inadequate to handle the significantly higher heat fluxes expected in an FNSF, or DEMO. The snowflake divertor configuration [44] enables edge magnetic shear, divertor plasma-wetted area, connection length and divertor volumetric losses to increase beyond those of the standard divertor configuration. This configuration, enhanced by radiative detachment, has demonstrated a significant reduction in both steady-state and ELM divertor heat fluxes, high core plasma confinement with reduced core impurities, and stable operation. The plasma-wetted area is increased up to 200%, X-point connection length 50-100%, and the divertor volume up to 60%. The peak divertor heat flux decreased from 7 to less than 1 MW/m^2 [45] between ELMs. Core H-mode confinement with τ_E~50-60 ms, plasma stored energy of 200-250 kJ, and H98(y,2) ~ 1 was maintained, and core and edge carbon concentration was reduced by up to 50%. During snowflake configuration operation, Type I ELMs stabilized by pedestal changes linked to the use of lithium (section 3.1) re-appeared [46]. Heat fluxes from Type I ELMs ($\Delta W_{plasma}/W_{plasma}$ = 7-10 %) were significantly dissipated (FIG. 16). Peak target temperatures, measured by fast infrared thermography during ELMs, reached 1000-1200 ^{o}C in the standard divertor and only 300-500 ^{o}C in the snowflake configuration. This was consistent with the lower surface temperature rise due to the longer convective heat deposition time due to the longer L_x in the snowflake divertor, and the convective heat redistribution mechanism in the null-point region proposed theoretically [47]. The snowflake was maintained during ELMs. In NSTX-U, two up-down symmetric sets of four divertor coils will be used to test snowflake divertors for handling the projected steady-state peak divertor heat fluxes of 20-30 MW/m^2 in I_p = 2 MA plasmas with up to 12 MW NBI heating.

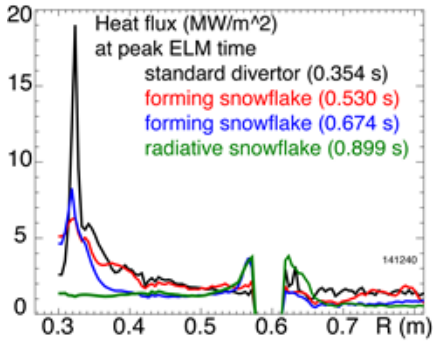

FIG. 16. Peak divertor heat flux for standard and snowflake divertors during Type I ELMs.

6.2. Effects of Non-axisymmetry and 3D fields

Application of 3D fields is a leading technique for MHD mode control, including ELMs, and to control plasma rotation. Therefore, 3D field application and heat flux reduction techniques must be compatible. Toroidal asymmetry of heat deposition is observed during ELMs, or by application of 3D fields. The asymmetries in the toroidal distribution of peak heat flux, q_{peak}, and heat flux width, λ_q, become largest at the peak of the ELM heat flux [48]. This is a serious

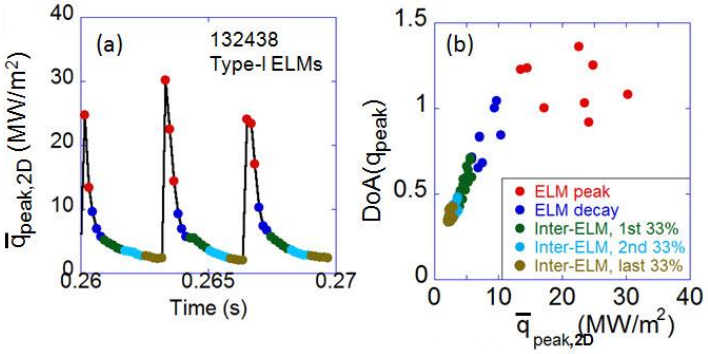

FIG. 17. (a) Evolution of measured mean peak heat flux during type-I ELMs (b) Toroidal degree of asymmetry for q_{peak} during ELM activity.

concern for first wall tile design and cooling requirements, which are usually based on a 2D axisymmetric calculations. While the asymmetry caused by the applied 3D fields can re-attach a partially detached radiative divertor plasma due to an increase in pedestal T_e, additional gas puffing can restore detachment [49]. Applied 3D field pulses with amplitudes below ELM triggering level show increased D_α intensity, indicating increased particle transport. Measured strike point splitting is qualitatively reproduced by EMC3-Eirene modelling [50].

7. Non-Inductive Current Results and Operational Scenarios for NSTX-U

7.1. Co-axial Helicity Injection

Transient Coaxial Helicity Injection (CHI) has generated 300 kA peak toroidal current and 200kA on closed flux surfaces without the use of the central solenoid. When induction from the solenoid was added to CHI start-up, plasmas ramped to 1MA required 35% less inductive flux. These discharges have high elongation ~ 2.6, low plasma density and l_i ~ 0.35 desirable for achieving advanced scenarios [51]. Full discharge simulations using the TSC code, including CHI and subsequent current ramp-up using neutral beams, show favourable scaling of the CHI start-up process with increasing machine size. This analysis predicts at least a doubling of the closed flux current for NSTX-U [52].

7.2. Non-inductive Current Results, and Fully Non-inductive Scenarios for NSTX-U

H-mode plasmas with I_p = 0.3MA, B_T = 0.55 T, and 1.4 MW of 30 MHz high-harmonic fast wave (HHFW) power with current drive phasing have reached a non-inductive plasma current fraction (NICF) of 70 – 100% as computed by TRANSP-TORIC analysis. With an estimated RF coupling efficiency of 60%, direct RF-driven current is 60 - 70 kA. The computed bootstrap current fluctuates from 100 to 230 kA. The current generated directly by HHFW power was inside a normalized minor radius ~ 0.2, and 75% of the non-inductive current was generated inside a normalized minor radius ~ 0.4 [53]. Over the entire range of NBI heated plasmas, up to 65% NICF was experimentally reached (computed by TRANSP), peaking at plasma current value of I_p = 0.7 MA.

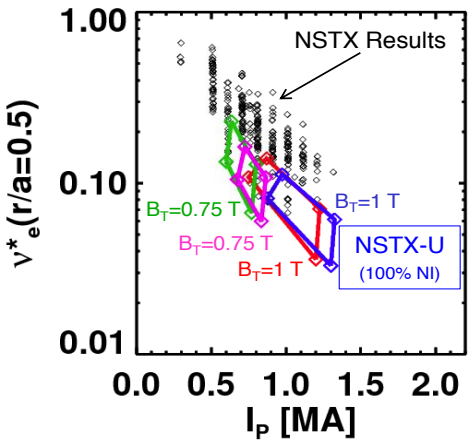

FIG. 18. Projected (I_p, ν_e^*) operation space in NSTX-U with 100% NICF.

Significant progress has been made on the present hardware upgrade of NSTX. A major milestone for NSTX-U (and a decades-long goal for tokamak operation in general) is routine operation at 100% non-inductive fraction. Such operation is expected to bring new challenges and opportunities for understanding tokamak transport and stability. Routine operation of NSTX at high non-inductive current fraction allows confident projection to potential 100% non-inductive operational scenarios for NSTX-U. Experimental scenario development in NSTX has already accessed aspect ratio (up to 1.73) and boundary shaping (elongation greater than 2.9) planned for NSTX-U [54]. Predictive TRANSP calculations project 100% NIC fraction over a wide range of I_p from 0.6 – 1.35 MA, capability for an order of magnitude collisionality variation, and a factor of 4 reduction in ν^*_e compared to

NSTX for fully relaxed plasmas with $q_{min} > 1$ (FIG. 18). The scenarios shown considered B_T from 0.75 T to the maximum planned value of 1 T, and are limited to 75% of the Greenwald density limit.

This research was funded by the United States Department of Energy under contract DE-AC02-09CH11466.

---

[1] PENG, Y.K.-M., BURGESS, T.W., CARROLL, A.J., et al., Fusion Sci. Technol. **56** (2009) 957.
[2] PENG, Y.K.-M, FOGARTY, P.J., BURGESS, T.W., et al., Plasma Phys. Control. Fusion **47** (2005) B263.
[3] MENARD, J.E., BROMBERG, L., BROWN, T., et al., Nucl. Fusion **51** (2011) 103014.
[4] WILSON, H.R., AHN, J., AKERS, R., Nucl. Fusion **44** (2004) 917.
[5] MENARD, J.E., GERHARDT, S., BELL, M., et al., Nucl. Fusion **52** (2012) 083015.
[6] BELL, M.G., et al., Plasma Phys. Controlled Fusion **51** (2009) 124054.
[7] KAYE, S.M., et al., Proc. 24th Int. Conf. on Fusion Energy (San Diego, USA, 2012) paper EX/7-1.
[8] GUTTENFELDER, W., et al. Proc. 24th Int. Conf. on Fusion Energy (San Diego, USA, 2012) paper TH/6-1.
[9] GUTTENFELDER, W., CANDY, J., KAYE, S.M., et al., Phys. Plasmas **19** (2012) 056119.
[10] REN, Y., et al., Phys. Plasmas **19** (2012) 056125.
[11] REN, Y., et al., Proc. 24th Int. Conf. on Fusion Energy (San Diego, USA, 2012) paper EX/P7-02.
[12] YUH, H., et al., Phys. Rev. Lett. **106** (2011) 055003.
[13] PETERSON, J.L., Phys. Plasmas **19** (2012) 056120.
[14] SABBAGH, S.A., BERKERY, J.W., BELL, R.E., Nucl. Fusion **50** (2010) 025020.
[15] BERKERY, J.W., SABBAGH, S.A., BETTI, R., et al., Phys. Rev. Lett. **104** (2010) 035003.
[16] BERKERY, J.W., SABBAGH, S.A., BETTI, R., et al., Phys. Rev. Lett. **106** (2011) 075004.
[17] REIMERDES, H., CHU, M., GAROFALO, A., et al., Phys. Rev. Lett. **93** (2004) 135002.
[18] BERKERY, J.W., et al., Proc. 24th Int. Conf. on Fusion Energy (San Diego, USA, 2012) paper EX/P8-07.
[19] MAINGI, R., KAYE, S.M., SKINNER, C.H., et al., Phys. Rev. Lett. **107** (2011) 145004.
[20] PODESTA, M., et al., Proc. 24th Int. Conf. on Fusion Energy (San Diego, USA, 2012) paper EX/P3-02.
[21] CANIK, J., et al., Proc. 24th Int. Conf. on Fusion Energy (San Diego, USA, 2012) paper EX/P7-16.
[22] BOYLE, D.P., MAINGI, R., SYNDER, P., et al., Plasma Phys. Control. Fusion **53** (2011) 105011.
[23] MAINGI, R., et al., Proc. 24th Int. Conf. on Fusion Energy (San Diego, USA, 2012) paper EX/11-2.
[24] JAWORSKI, M., et al., Proc. 24th Int. Conf. on Fusion Energy (San Diego, USA, 2012) paper EX/P5-31.
[25] KRSTIC, P., ALLAIN, J., TAYLOR, C., et al., submitted to Nature Comm. (2012).
[26] CHANG, C.S., et al., Proc. 24th Int. Conf. on Fusion Energy (San Diego, USA, 2012) paper TH/P4-12.
[27] SNYDER, P., GROEBNER, R.J., HUGHES, J.W., et al., Nucl. Fusion **51** (2011) 103016.
[28] DIALLO, A., et al., Proc. 24th Int. Conf. on Fusion Energy (San Diego, USA, 2012) paper EX/P4-04.
[29] SMITH, D.R., et al., Rev. Sci. Instrum. **81** (2010) 10D717.
[30] SMITH, D.R., et al., Proc. 24th Int. Conf. on Fusion Energy (San Diego, USA, 2012) paper EX/P7-18.
[31] CROCKER, N.A., et al., Plasma Phys. Controll. Fusion **53** (2011) 105001.
[32] KU, S-H., CHANG, C.S., DIAMOND, P.H., et al., Nucl. Fusion **49** (2009) 115021.
[33] SABBAGH, S.A, SONTAG, A.C., BIALEK, J., et al., Nucl. Fusion **46** (2006) 635.
[34] GERHARDT, S.P., et al., Proc. 24th Int. Conf. on Fusion Energy (San Diego, USA, 2012) paper EX/9-3.
[35] LA HAYE, R.J., BUTTERY, R., GERHARDT, et al., Phys. Plasmas **19** (2012) 062506.
[36] PARK, J-K., et al., Proc. 24th Int. Conf. on Fusion Energy (San Diego, USA, 2012) paper EX/P4-33.
[37] SABBAGH, S.A., KATSURO-HOPKINS, O., BIALEK, J., submitted to Phys. Rev. Lett.
[38] ABDELAZIZ, T.H.S.,VALASEK, M., Proc 16th IFAC World Congress, Prague (2005).
[39] KATSURO-HOPKINS, O., BIALEK, J., MAURER, D., et al., Nucl. Fusion **47** (2007) 1157.
[40] GERHARDT, S.P., MENARD, J.M., SABBAGH, S.A., et al., Nucl. Fusion. **52** (2012) 063005.
[41] FREDRICKSON, E., et al., Proc. 24th Int. Conf. on Fusion Energy (San Diego, USA, 2012) paper EX/P6-05.
[42] BERKERY, J.W., SABBAGH, S.A., REIMERDES, H., et al., Phys. Plasmas **17** (2010) 082504.
[43] CROCKER, N., et al., Proc. 24th Int. Conf. on Fusion Energy (San Diego, USA, 2012) paper EX/P6-02.
[44] RYUTOV, D. D., Phys. Plasmas **14** (2007) 064502.
[45] SOUKHANOVSKII, V.A., BELL, R.E., DIALLO, A., Phys. Plasmas **19** (2012) 082504.
[46] SOUKHANOVSKII, V.A., et al., Proc. 24th Int. Conf. on Fusion Energy (San Diego, USA, 2012) EX/P5-21.
[47] RYUTOV, D.D., et al., Proc. 24th Int. Conf. on Fusion Energy (San Diego, USA, 2012) paper TH/P4-18.
[48] AHN, J-W., et al., Proc. 24th Int. Conf. on Fusion Energy (San Diego, USA, 2012) paper EX/P5-33.
[49] AHN, J-W., MAINGI, R., CANIK, J.M., et al., Phys. Plasmas **18** (2011) 056108.
[50] LORE, J.D., CANIK, J.M., FENG, Y., et al., Nucl. Fusion **52** (2012) 054012.
[51] RAMAN, R., MUELLER, D., JARBOE, T.R., et al., Phys. Plasmas **18** (2011) 092504.
[52] RAMAN, R., et al., Proc. 24th Int. Conf. on Fusion Energy (San Diego, USA, 2012) paper EX/P2-10.
[53] TAYLOR, G., et al., Phys. Plasmas **19** (2012) 042501.
[54] GERHARDT, S.P., GATES, D.A., KAYE, S.M., et al., Nucl. Fusion **51** (2011) 073031.